Article

Discovery Medicine 2025; 37(200): 2041–2054
https://doi.org/10.24976/Discov.Med.202537200.175

The E3 Ubiquitin Ligase MIB2 Exacerbates Sepsis-Associated Acute Kidney Injury by Promoting GPX4 Degradation-Mediated Ferroptosis and Mitochondrial Dysfunction

Lihua Tang[1,†], Feng Zhou[1,†], Yufei Wang[1], Yuxia Jiao[1,*]

[1]Department of Anesthesiology, The Second Hospital of Dalian Medical University, 116027 Dalian, Liaoning, China
*Correspondence: jiao_510@163.com (Yuxia Jiao)
[†]These authors contributed equally.
Submitted: 17 July 2025 Revised: 20 August 2025 Accepted: 26 August 2025 Published: 20 September 2025

Background: Sepsis-associated acute kidney injury (SA-AKI) is a critical clinical complication with high mortality, involving ferroptosis and mitochondrial dysfunction, although the regulatory mechanisms remain incompletely defined. E3 ubiquitin ligases play key roles in post-translational regulation of cell death pathways, but their specific involvement in SA-AKI-associated ferroptosis is poorly understood. This study aimed to investigate the role and mechanism of the E3 ubiquitin ligase mind bomb 2 (MIB2) in SA-AKI, focusing on its regulation of ferroptosis and mitochondrial function via glutathione peroxidase 4 (GPX4).
Methods and Materials: An SA-AKI model was established by treating HK-2 cells with different concentrations of lipopolysaccharide (LPS). Cell viability was detected using the cell counting kit-8 (CCK-8) assay. The mRNA and protein expression levels of MIB2 and GPX4 were detected using reverse-transcription polymerase chain reaction (RT-qPCR) and Western blotting (WB). The interaction between MIB2 and GPX4 was verified by co-immunoprecipitation (Co-IP). An MIB2 knockdown model was constructed by means of sh-MIB2 transfection. The MIB2 knockdown model treated with ras-selective lethal small molecule 3 (RSL3), a GPX4 inhibitor, was subjected to the detection of reactive oxygen species (ROS), glutathione (GSH), Fe^{2+}, and malondialdehyde (MDA) by means of flow cytometry and assay kits. To evaluate mitochondrial function, the mitochondrial morphology, membrane potential, and adenosine triphosphate (ATP) content were analyzed via transmission electron microscopy, JC-1 staining, and chemiluminescence.
Results: LPS reduced the viability of HK-2 cells in a manner dependent on both concentration and time, significantly increased the mRNA and protein levels of MIB2 ($p < 0.001$), and simultaneously decreased the mRNA and protein levels of GPX4 ($p < 0.001$). Co-IP confirmed a direct interaction between MIB2 and GPX4. Knocking down MIB2 could significantly reverse the down-regulation of GPX4 induced by LPS ($p < 0.001$), and reduced the levels of intracellular reactive oxygen species (ROS), Fe^{2+} and MDA, accompanied by glutathione (GSH) depletion and lipid ROS accumulation. MIB2 knockdown also improved mitochondrial morphological aberrations (increased proportion and length of intact cristae), increased mitochondrial membrane potential and ATP content, and enhanced cell viability ($p < 0.001$). Treatment with RSL3 could reverse the up-regulation effect of MIB2 knockdown on GPX4 and the protective effects on ferroptosis and mitochondrial function.
Conclusions: The E3 ubiquitin ligase MIB2 induces ferroptosis and mitochondrial dysfunction in HK-2 cells by binding to GPX4 and promoting its degradation, thus exacerbating SA-AKI. MIB2 knockdown can alleviate these pathological processes by stabilizing GPX4.

Keywords: MIB2; GPX4; ferroptosis; mitochondrial function; sepsis-associated acute kidney injury

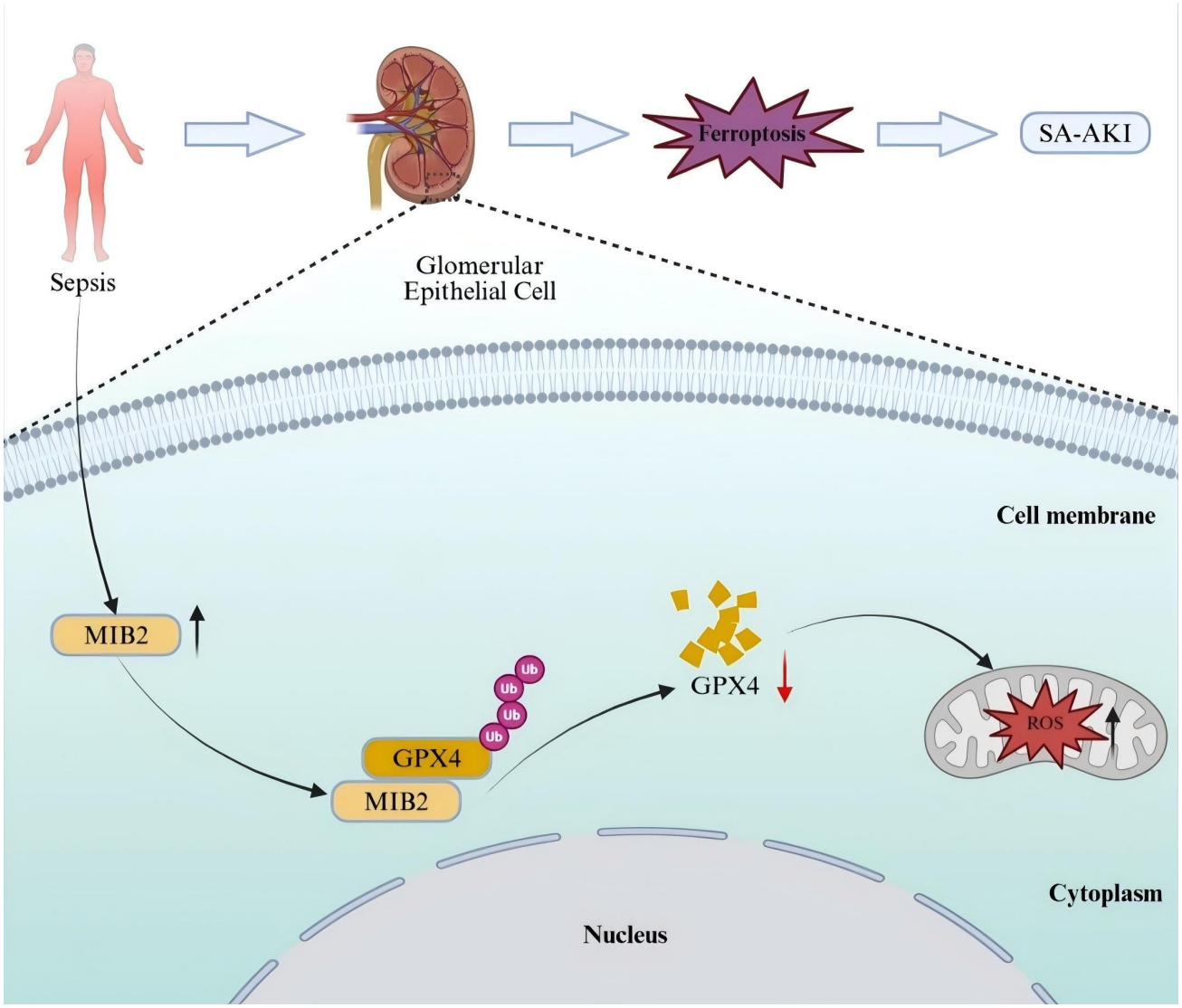

Graphical Abstract.

Introduction

Sepsis is a life-threatening syndrome characterized by an uncontrolled host response to infection, leading to multiorgan dysfunction and a mortality rate exceeding 30% in severe cases [1]. Overwhelming production of reactive oxygen species (ROS) in this condition causes oxidative damage and dysfunction in multiple organs, with the kidneys being particularly vulnerable, often leading to sepsis-associated acute kidney injury (SA-AKI) [2–4]. The reported occurrence rate of SA-AKI varies from 25% to 75% [5]. Those with sepsis-associated AKI face a 3- to 5-fold increase in 60-day mortality compared to non-AKI patients, and the mortality rate for SA-AKI is significantly higher than for non-septic AKI [6–8]. While much emphasis was placed on researching effective preventive and treatment approaches for SA-AKI, their therapeutic outcomes are often less than satisfactory, as pathological mechanisms remain largely unclear. Thus, investigating these mechanisms are vital for improving prevention and treatment of SA-AKI, as well as patient prognosis.

Ferroptosis is an iron-dependent form of regulated cell death, which is biologically and morphologically distinct from apoptosis, necrosis, and autophagy. Its hallmark is iron-dependent lipid peroxidation of membrane unsaturated fatty acids, catalyzed by divalent iron or lipoxygenases, ultimately leading to cell membrane damage and cell death [9,10]. During ferroptosis, antioxidants, including glutathione (GSH) and glutathione peroxidase 4 (GPX4), show reduced expression [11–13].

Ubiquitination, a pivotal post-translational modification, involves the covalent attachment of ubiquitin to target proteins via the concerted action of ubiquitin-activating, ubiquitin-conjugating, and ubiquitin-ligating enzymes [14–16]. Dysregulation of this ubiquitin-proteasome-mediated regulatory pathway has been implicated in an array of pathological states, including non-small cell lung cancer, hepatocellular carcinoma, breast malignancies, skeletal disorders, and ischemia/reperfusion-mediated acute kidney injury, often in conjunction with aberrant ferroptotic signaling [17–20].

Mind bomb 2 (MIB2) is an E3 ligase that targets the Notch1 protein for ubiquitination [21]. At current stage, however, not much is known about the role of MIB2 in kidney diseases, and whether it affects ferroptosis and mitochondrial function in SA-AKI by regulating GPX4 through ubiquitination remains to be confirmed. Notably, while ferroptosis and GPX4 ubiquitination are critical in SA-AKI, the specific E3 ligases mediating GPX4 degradation in this context remain unclear. Additionally, MIB2's function in renal diseases, especially its potential role in regulating GPX4, ferroptosis, or mitochondrial dysfunction during SA-AKI, has never been explored.

In this study, we investigated whether MIB2 acts as an E3 ligase to regulate GPX4 via ubiquitination, thereby influencing ferroptosis, mitochondrial function, and SA-AKI progression. Our work identified a novel MIB2-GPX4 axis, filling a key knowledge gap in the SA-AKI pathogenesis. Herein, we hypothesized that MIB2, as an E3 ubiquitin ligase, may regulate GPX4 ubiquitination and degradation, thereby inducing ferroptosis and exacerbating SA-AKI. This study aims to clarify this mechanism and explore the potential of targeting MIB2 as a therapeutic strategy for SA-AKI.

Materials and Methods

Cell Culture and Cell Transfection

The HK-2 cells (CL-0109, Procell Life Science & Technology Co., Ltd., Wuhan, China) were used in the study. The HK-2 cells were identified through short tandem repeat (STR) profiling, and no mycoplasma was detected. The cells were cultivated in high-glucose Dulbecco's Modified Eagle Medium (DMEM, Cat# 11965092, Gibco, Thermo Fisher Scientific, Waltham, MA, USA) supplemented with 10% fetal bovine serum (FBS, Cat# 10099141C, Gibco, Thermo Fisher Scientific, Waltham, MA, USA) and 1% penicillin-streptomycin (PS, Cat# 15140122, Gibco, Thermo Fisher Scientific, Waltham, MA, USA). At 37 °C, the culture was preserved in a humidified setting with 5% carbon dioxide. The shRNA targeting MIB2 (sh-MIB2) and a negative control shRNA (sh-NC) for use in the cell transfection experiments were sourced from Nanyang Oulinge Biotechnology Co., Ltd. (Nanyang, Henan, China), with sequences listed in the following: (1) sh-MIB2-1: sense 5′-CGCAGUGCUACAUGCACAACA-3′, anti-sense 5′-UUGUGCAUGUAGCACUGCGUG-3′; (2) sh-MIB2-2: sense 5′-CGCACGACCUGCUGCUGUACG-3′, anti-sense 5′-UACAGCAGCAGGUCGUGCGCG-3′; (3) sh-MIB2-3: sense 5′-GUGUGUGCCUGGACUACGACC-3′, anti-sense 5′-UCGUAGUCCAGGCACACACGG-3′; and (4) sh-NC: sense 5′-UUCUCCGAACGUGUCACGUTT-3′, anti-sense 5′-ACGUGACACGUUCGGAGAATT-3′. The three sh-MIB2 sequences were tested to determine the most optimal sequence that delivers the best off-target effects and efficient knockdown of MIB2 mRNA and protein, verified by quantitative reverse-transcription polymerase chain reaction (RT-qPCR) and Western blotting (WB). Following the manufacturer's guidelines, HK-2 cells were seeded in 6-well plates (Cat# 3516, Corning Inc., Corning, NY, USA). Upon reaching 50% confluence, the cells were transfected with 50 nM sh-MIB2 or sh-NC using Lipofectamine 3000 (Cat# L3000015, Invitrogen, Thermo Fisher Scientific, Waltham, MA, USA).

RSL3 (Cat# HY-100218A, MedChemExpress, Monmouth Junction, NJ, USA) was prepared as a 10 mM stock solution in dimethyl sulfoxide (DMSO, Cat# D2650, Sigma-Aldrich, Merck KGaA, Darmstadt, Germany) and diluted to a final working concentration of 3 μM in com-

plete medium. For groups requiring RSL3 treatment (LPS+sh-MIB2+RSL3 and LPS+sh-NC+RSL3), RSL3 was added to HK-2 cells 24 hours after shRNA transfection and maintained for 24 hours. During this period, lipopolysaccharide (LPS, Cat# L2880, Sigma-Aldrich, Merck KGaA, Darmstadt, Germany; 4.5 µg/mL) was co-administered with RSL3 to ensure simultaneous stimulation, and the medium was not refreshed to avoid disrupting the 24-hour treatment window.

The overall timeline for MIB2 knockdown experiments was as follows: (1) HK-2 cells were seeded and cultured to 50% confluence (18–24 hours); (2) transfected with sh-MIB2 or sh-NC; (3) cultured for 24 hours to stabilize transfection; (4) treated with LPS (4.5 µg/mL) alone or in combination with RSL3 (3 µM) at 24 hours post-transfection; (5) maintained for 24 hours before sample collection for downstream assays.

CCK-8 Assay

HK-2 cells were treated with various LPS concentrations (0.56, 1.12, 2.25, 4.5, and 9 µg/mL) [13,22]. A 3 mg/mL LPS stock solution was prepared by dissolving 3 mg of LPS powder in 1 mL of DMSO. The LPS solution was diluted in complete medium to the desired concentrations, and cells were treated accordingly. After 24, 48, or 72 hours, a CCK-8 assay (Cat# C0038, Beyotime Biotechnology, Shanghai, China) was performed. Each well received 20 µL of CCK-8 reagent, and the cells were incubated in the dark at 37 °C for 1 to 4 hours. A microplate reader (Synergy H1, Epoch 2, BioTek Instruments, Winooski, VT, USA) was used to measure the optical density (OD) at 450 nm to evaluate the effects of various LPS concentrations on cell growth, while cell morphology was examined with an inverted light microscope (Olympus IX73, Olympus Corporation, Tokyo, Japan) at 100× magnification.

RT-qPCR Analysis

Total RNA was extracted from HK-2 cells at 48 hours post-transfection using TRIzol reagent (Cat# 15596026, Invitrogen, Thermo Fisher Scientific, Waltham, MA, USA). The RNA's concentration and purity were evaluated using a NanoDrop 2000 spectrophotometer (Thermo Fisher Scientific, Waltham, MA, USA). For cDNA synthesis, 1 µg of total RNA was reverse-transcribed using a PrimeScript RT Master Mix (Cat# RR036A, Takara Bio Inc., Shiga, Japan) with gDNA Eraser to eliminate genomic DNA contamination. The StepOnePlus Real-Time PCR System (Applied Biosystems, Thermo Fisher Scientific, Waltham, MA, USA) was used to perform RT-qPCR. The primer sequences for *MIB2*, *GPX4*, *GAPDH* (internal control) are shown in Table 1. Relative mRNA expression levels were calculated using the $2^{-\Delta\Delta Ct}$ method, normalized to the internal reference gene *GAPDH*.

Detection of ROS Level

The HK-2 cells were adjusted to a density of 5×10^5 cells/mL, placed in a 6-well plate with 2 mL in each well, and incubated at 37 °C with 5% CO_2 for a duration of 24 hours. Cells were exposed to LPS at a final concentration of 4.5 µg/mL and maintained in culture for 72 hours before cell harvesting for subsequent analysis. For ROS detection, the cells were collected and processed as follows:

To detect total intracellular ROS, DCFH-DA (Cat# S0033S, Beyotime Biotechnology, Shanghai, China) was diluted to 10 µM in serum-free medium (1:1000 ratio). The cells (1–20 million cells/mL) were incubated with the diluted DCFH-DA probe reagent for 20 minutes, with gentle mixing every 5 minutes. To detect oxidized lipids, C11-BODIPY probe (Cat# D3861, Invitrogen, Thermo Fisher Scientific, Waltham, MA, USA) was diluted to 5 µM in serum-free medium (1:1000 ratio). The cells were incubated with the probe reagent at 37 °C in the dark for 30 minutes. After incubation with either probe reagent, the cells were washed three times with serum-free medium to remove unbound probes. Samples were analyzed via flow cytometry (oxidized lipids was monitored by the shift from red to green fluorescence), and data were processed with FlowJo 7.6 software (v7.6, FlowJo LLC, Ashland, OR, USA).

Iron Detection

The intracellular iron levels were measured using a commercial iron assay kit (Cat# ab83366, Abcam, Cambridge, UK). All materials were equilibrated to 20 °C–25 °C. For sample pretreatment, 3×10^6 cells were added to 150 µL of buffer and subjected to 400 Amps for 5 seconds per cycle, repeated 3–5 times, then centrifuged at 1200 rpm for 10 minutes. The supernatant was collected for measurement. A 1 mM iron standard solution was prepared by diluting 10 µL of 100 mM standard reagent in 990 µL of double-distilled water. Reaction wells were prepared by adding 25 µL of sample. Each standard well received 5 µL of iron-reducing reagent, and each sample well received 5 µL of buffer. Following mixing, the standards and samples were kept at 37 °C for 30 minutes, after which 100 µL of iron probe was added and incubated in the dark for an additional 60 minutes.

Transmission Electron Microscopy (TEM)

Prior to TEM analysis, the cells were prepared as follows: first fixed in 2.5% glutaraldehyde (Cat# G5882, Sigma-Aldrich, Merck KGaA, Darmstadt, Germany) in 0.1 M PBS (pH 7.4) for 3 hours at room temperature to stabilize ultrastructure. They were then gently scraped (to avoid damage), centrifuged at 1500 ×g for 5 minutes at 4 °C, refixed in the same glutaraldehyde for 1 hour, and post-fixed in 1% osmium tetroxide (0.1 M PBS) for 1.5 hours at 4 °C. After 3 PBS washes (15 minutes each), cells were dehydrated via graded ethanol, infiltrated with epoxy

Table 1. List of primer sequences.

Gene	Sequences	
	Forward (5′–3′)	Reverse (5′–3′)
MIB2	AGCGGGCGGCTTCTACTA	GCGGTCCGTGATACGATG
GPX4	GTGAGGCAAGACCGAAGT	TCCCGAACTGGTTACACG
GAPDH	GGAGCGAGATCCCTCCAAAAT	GGCTGTTGTCATACTTCTCATGG

MIB2, mind bomb 2; *GPX4*, glutathione peroxidase 4; *GAPDH*, Glyceraldehyde-3-phosphate dehydrogenase. All primers were synthesized by Sangon Biotech Co., Ltd. (Shanghai, China).

resin, embedded, polymerized at 60 °C for 48 hours, sectioned into 60–80 nm slices, stained with uranyl acetate (Cat# 21447, Electron Microscopy Sciences, Hatfield, PA, USA) and lead citrate (Cat# 17800, Electron Microscopy Sciences, Hatfield, PA, USA), air-dried, and imaged using a Hitachi HT7700 TEM at 120 kV.

Western Blotting (WB)

Proteins were extracted from HK-2 cells with a RIPA buffer containing protease and phosphatase inhibitors, and their concentration was measured using a BCA protein assay kit (Cat# P0012, Beyotime Biotechnology, Shanghai, China). Electrophoresis was performed on a 10% SDS-PAGE gel with 50 µg of protein samples, which were then transferred to a PVDF membrane (Cat# IPVH00010, Millipore, Merck KGaA, Darmstadt, Germany). The membrane was incubated overnight at 4 °C with primary antibodies against GPX4 (1:1000, Cat# DF6701, Affinity Biosciences, Changzhou, China) and GAPDH (1:2000, Cat# ab181602, Abcam, Cambridge, UK) after being blocked with 5% non-fat dry milk. Subsequently, the membrane was incubated with HRP-labeled Goat Anti-Rabbit IgG H&L (1:2500, Cat# ZB-2301, ZSGB-BIO, Beijing, China) for 2 hours at room temperature following TBST washes. An ECL system (Cat# CJ600, Applygen Technologies, Beijing, China) was used to visualize the bands, and BandScan software (v5.0, GlycoBiosciences, Toronto, ON, Canada) was employed to analyze their intensities [23].

Co-IP Assay

To verify the direct interaction between MIB2 and GPX4 and investigate MIB2-mediated ubiquitination of GPX4, Co-IP assays were performed. HK-2 cells were lysed in IP lysis buffer (Cat# P0012, Beyotime Biotechnology, Shanghai, China) containing protease inhibitors (Complete Mini, Cat# 11836153001, Roche, Basel, Switzerland) on ice for 30 minutes. Lysates underwent centrifugation at 12,000 $\times g$ for 15 minutes at 4 °C, and the supernatant was obtained. In the immunoprecipitation process, 500 µg of total protein was incubated with 2 µg of anti-GPX4 antibody (1:2000, Cat# 14432-1-AP, Proteintech, Wuhan, China) or IgG control (1:100, Cat# ab172730, Abcam, Cambridge, UK) overnight at 4 °C while gently rotating. After adding Protein A/G agarose beads (Cat# sc-2003, Santa Cruz Biotechnology, Dallas, TX, USA), the incubation was extended for another 4 hours at 4 °C. Following five washes with cold IP buffer, the bound proteins on the beads were eluted by boiling in 2× SDS loading buffer for 10 minutes. The eluted proteins were then subjected to Western blot analysis. Primary antibodies against ubiquitin (1:1000, Cat# #20326, CST, Danvers, MA, USA), and GPX4 (1:2000, Cat# 14432-1-AP, Proteintech, Wuhan, China) were added to the membrane, followed by incubation at 4 °C overnight with gentle shaking to ensure specific binding. After washing with Tris-buffered saline containing 0.1% Tween-20 (TBST) three times (10 minutes each), HRP-labeled Goat Anti-Rabbit IgG H&L (1:2500, Cat# ZB-2301, ZSGB-BIO, Beijing, China) was used as the secondary antibody, and the membrane was incubated with it at room temperature (25 ± 2 °C) for 1.5 hours with gentle shaking. As a control, input samples containing 10% of the total protein were included.

ELISA Detection

Levels of MDA and GSH were quantified using an enzyme-linked immunosorbent assay (ELISA) kit (Cat# ab118970 and Cat# ab239709, Abcam, Cambridge, UK). RIPA buffer (Cat# P0013B, Beyotime Biotechnology, Shanghai, China)was used to lyse HK-2 cells, and the cell lysate was then subjected to centrifugation at 12,000 $\times g$ for 10 minutes. Supernatants were collected after centrifugation for subsequent analyses. Samples and standards were incubated in a pre-coated microplate (Abcam, Cambridge, UK) at 37 °C for 2 hours, followed by sequential incubations with biotinylated antibody (1 hour at 37 °C), streptavidin-HRP (30 min at 37 °C), and TMB substrate (15 minutes). After stopping the reaction, absorbance at 450 nm was measured, and concentrations were determined by reference to the standard curve plotted.

JC-1 Staining for Mitochondrial Membrane Potential

Mitochondrial membrane potential was detected using a JC-1 Assay Kit (Cat# C2006, Beyotime Biotechnology, Shanghai, China). HK-2 cells were seeded in 6-well plates and treated in accordance with the manufacturer's instructions provided with the JC-1 Assay Kit. After treatment, the cells were incubated with 10 µM JC-1 working dye solution at 37 °C for 20 minutes in the dark. After washing twice with JC-1 buffer, the cells were incubated with

Hoechst 33342 (1 µg/mL in PBS, Cat# C1022; Beyotime Biotechnology, Shanghai, China) at room temperature for 10 minutes in the dark to label nuclei. Afterward, the cells were washed three times with PBS. Fluorescence images were captured using a fluorescence microscope (Olympus IX73, Olympus Corporation, Tokyo, Japan) with excitation/emission wavelengths of 488 nm/530 nm (for JC-1 monomer, green fluorescence) and 543 nm/590 nm (for JC-1 aggregates, red fluorescence). The evaluation of mitochondrial membrane potential in terms of mitochondrial membrane potential ($\Delta\Psi m$) involved calculating the red-to-green fluorescence intensity ratio, with a lower ratio indicating a loss of membrane potential.

ATP Detection by Chemiluminescence

HK-2 cells were lysed using ATP lysis buffer (Cat# S0026, Beyotime Biotechnology, Shanghai, China), and subsequently centrifuged at 12,000 $\times g$ for 5 minutes to obtain the supernatants. A volume of 100 µL of ATP detection working solution (Cat# S0026; Beyotime Biotechnology, Shanghai, China) was added to a 96-well white plate, followed by 20 µL of sample or ATP standard. Luminescence intensity was measured immediately using a SpectraMax iD3 Multi-Mode Microplate Reader (Molecular Devices, San Jose, CA, USA). The standard curve was used to calculate ATP concentrations, which were then normalized to the protein concentration.

Statistical Analysis

Data are presented as mean ± standard deviation (SD) from at least three independent biological replicates (defined as experiments using distinct cell culture batches) for key assays (RT-qPCR, WB, ROS detection, etc.). A double-blind design was applied, in which both experimenters and analysts were blinded to group allocations to reduce bias. The Shapiro-Wilk test was used to assess the normality of data distribution. For cell viability experiments involving both concentration and time factors (Fig. 1A), two-way analysis of variance (ANOVA) was performed to evaluate the main effects and their interaction. To analyze differences among multiple groups, one-way ANOVA was employed, and Tukey's post hoc test was used for pairwise comparisons. The unpaired two-tailed Student's *t*-test was utilized for comparisons between two groups, with a $p < 0.05$ indicating statistical significance. Statistical analyses were conducted using GraphPad Prism version 8.0.1 (version 8.0.1, GraphPad Software, San Diego, CA, USA).

Results

Effect of LPS on the Viability of HK-2 Cells and the Expression Levels of MIB2 and GPX4

CCK-8 assay results (Fig. 1A) revealed that LPS inhibited HK-2 cell viability in a concentration- and time-dependent manner. Compared to those treated with 0 µg/mL LPS (control group), the cells treated with increasing LPS concentrations (0.56 µg/mL to 9 µg/mL) in an extended treatment duration (from 24 to 72 hours) experienced significantly lower viability, with the most pronounced effect observed at 9 µg/mL LPS for 72 hours ($p < 0.001$). RT-qPCR analysis (Fig. 1B) demonstrated that LPS treatment significantly upregulated *MIB2* mRNA expression and significantly downregulated *GPX4* mRNA expression in HK-2 cells ($p < 0.001$). Western blot results (Fig. 1C) were consistent with the mRNA expression trends, showing significantly increased MIB2 protein expression and significantly decreased GPX4 protein expression in the LPS-treated group ($p < 0.001$). Co-IP assays (Fig. 1D) further confirmed a direct interaction between MIB2 and GPX4 in the HK-2 cells. As shown in Fig. 1E, under LPS stimulation, GPX4 in the sh-NC group exhibited strong ubiquitination signals, whereas sh-MIB2 markedly reduced GPX4 ubiquitination, as observed in the immunoblot. Input blots confirmed that the total GPX4 protein levels were elevated in the sh-MIB2 group, consistent with reduced degradation. These data directly demonstrate that MIB2 enhances GPX4 ubiquitination, a key step in proteasomal degradation.

Effects of LPS on Ferroptosis and Mitochondrial Function-Related Indicators in HK-2 Cells

According to flow cytometry analysis (Fig. 2A,B), the LPS-treated group exhibited a significantly higher levels of intracellular ROS and lipid ROS compared to the control group ($p < 0.001$). Results from the iron assay kit (Fig. 2C) demonstrated a significant elevation in intracellular Fe^{2+} content in the LPS-treated group ($p < 0.001$). According to the ELISA results (Fig. 2D,E), LPS treatment significantly increased intracellular MDA content and decreased intracellular GSH content ($p < 0.001$), suggesting enhanced lipid peroxidation. TEM observation (Fig. 2F) revealed that LPS treatment induced abnormal mitochondrial morphology in HK-2 cells, characterized by reduced and disorganized mitochondrial cristae, whereas quantitative analysis (Fig. 2G) indicated that the proportion and length of mitochondria exhibiting intact dense cristae were significantly reduced in the LPS-treated group ($p < 0.001$). JC-1 staining results (Fig. 2H) demonstrated that LPS treatment significantly decreased the mitochondrial membrane potential (manifested as a reduced JC-1 aggregate/monomer ratio, $p < 0.001$). The intracellular ATP levels were significantly diminished in the LPS-treated group ($p < 0.001$), as shown by the chemiluminescence assay (Fig. 2I), suggesting mitochondrial function impairment.

Verification of the Transfection Efficiency of sh-MIB2 in HK-2 Cells

RT-qPCR analysis (Fig. 3A) demonstrated that the *MIB2* mRNA levels in the sh-MIB2 group cells were significantly reduced compared to the sh-NC group ($p <$

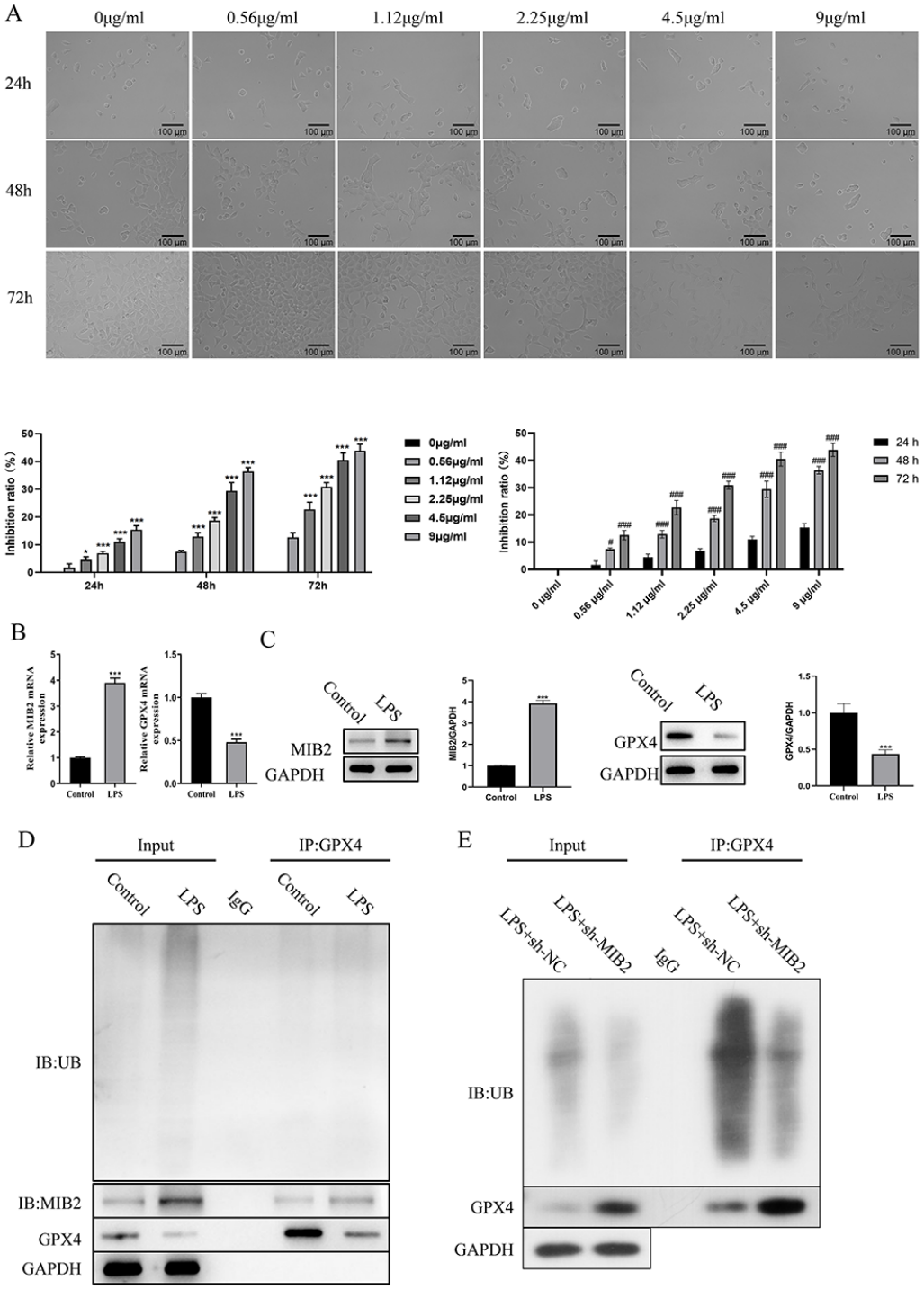

Fig. 1. Effects of LPS on HK-2 Cell Viability and Expression Levels of MIB2 and GPX4. (A) CCK-8 assay was used to detect the effects of different concentrations of LPS on HK-2 cell viability at 24, 48, and 72 h. Two-way ANOVA was performed to analyze the effects of concentration, time, and their interaction. Comparisons were made among different concentrations at the same time point, as well as across different time points within the same concentration. (B) RT-qPCR was used to detect the expression levels of *MIB2* and *GPX4* mRNA. (C) Western blot detection of expression levels of MIB2 and GPX4 proteins. (D) Co-IP detection of the binding relationship between MIB2 and GPX4. (E) GPX4 ubiquitination in LPS-treated HK-2 cells (sh-NC vs sh-MIB2) was detected by GPX4 immunoprecipitation and ubiquitin immunoblotting. IP: GPX4, Immunoblotting: Ubiquitin (IB: UB). (A) $*p < 0.05$, $***p < 0.001$ vs Control (0 μg/mL); $\#p < 0.05$, $\#\#\#p < 0.001$ vs. 24 h at the same concentration; (B–D) $***p < 0.001$ vs Control; $n = 3$. LPS, lipopolysaccharide; MIB2, mind bomb 2; GPX4, glutathione peroxidase 4; RT-qPCR, reverse-transcription polymerase chain reaction; Co-IP, co-immunoprecipitation; sh-NC, negative control shRNA.

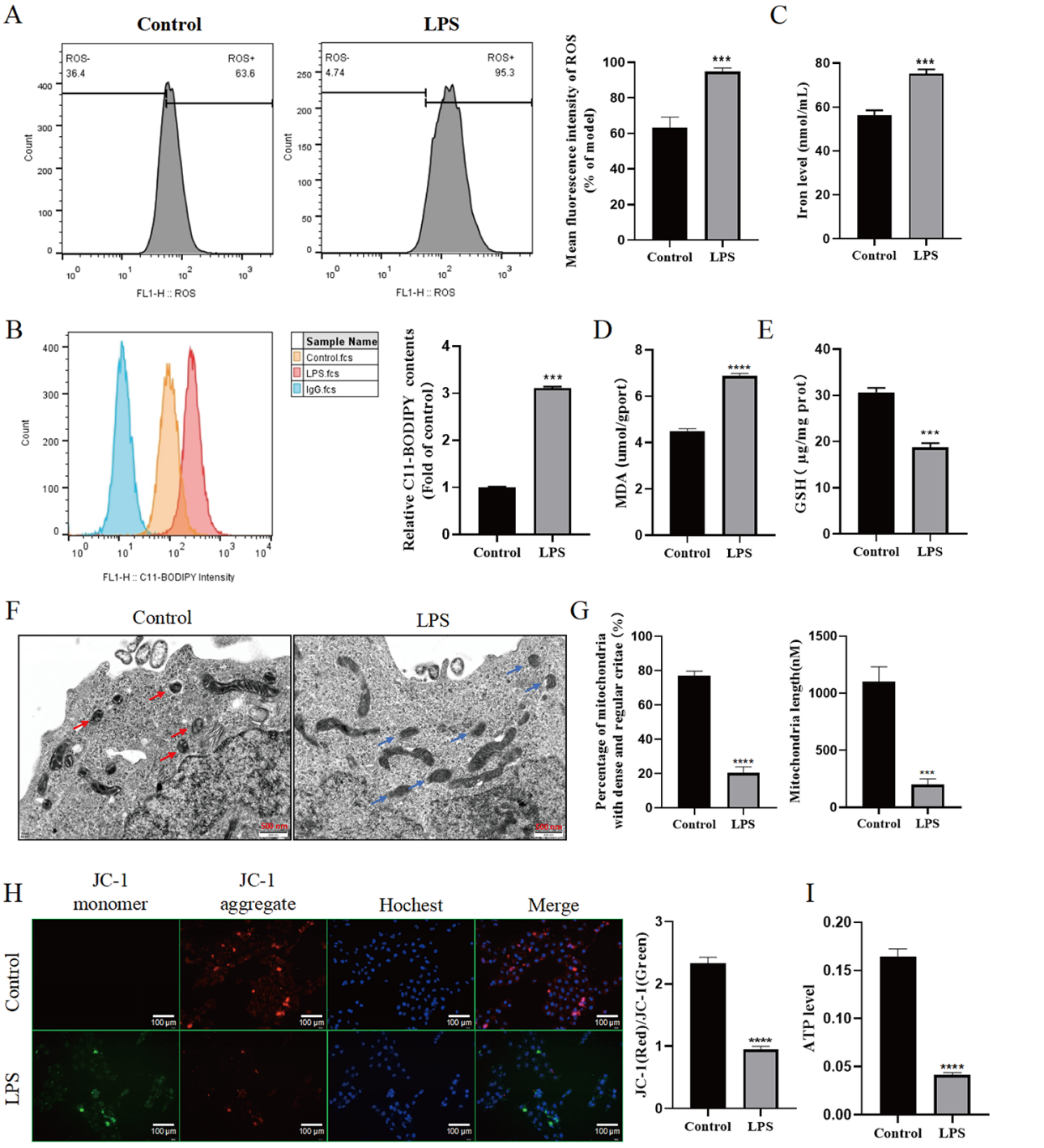

Fig. 2. The effect of LPS on ferroptosis and mitochondrial function-related indicators in HK-2 cells. (A) Flow cytometry analysis of total intracellular ROS levels in HK-2 cells using DCFH-DA probe. (B) Flow cytometry analysis of oxidized lipids levels in HK-2 cells using C11-BODIPY probe. (C) The iron detection kit detects the level of iron ions in HK-2 cells. (D,E) ELISA kit was used to detect the MDA and GSH content in HK-2 cells. (F) TEM observation of mitochondrial morphology in HK-2 cells. Red arrow: intact mitochondrial cristae; Blue arrow: disrupted cristae and swollen mitochondria. (G) The proportion and length of mitochondria with fine and dense cristae. (H) JC-1 staining was used to detect mitochondrial membrane potential. (I) Detection of intracellular ATP content using chemiluminescence method. ***$p < 0.001$, ****$p < 0.0001$ vs Control, $n = 3$. ROS, reactive oxygen species; ELISA, enzyme-linked immunosorbent assay; MDA, malondialdehyde; GSH, glutathione; TEM, transmission electron microscopy; ATP, adenosine triphosphate.

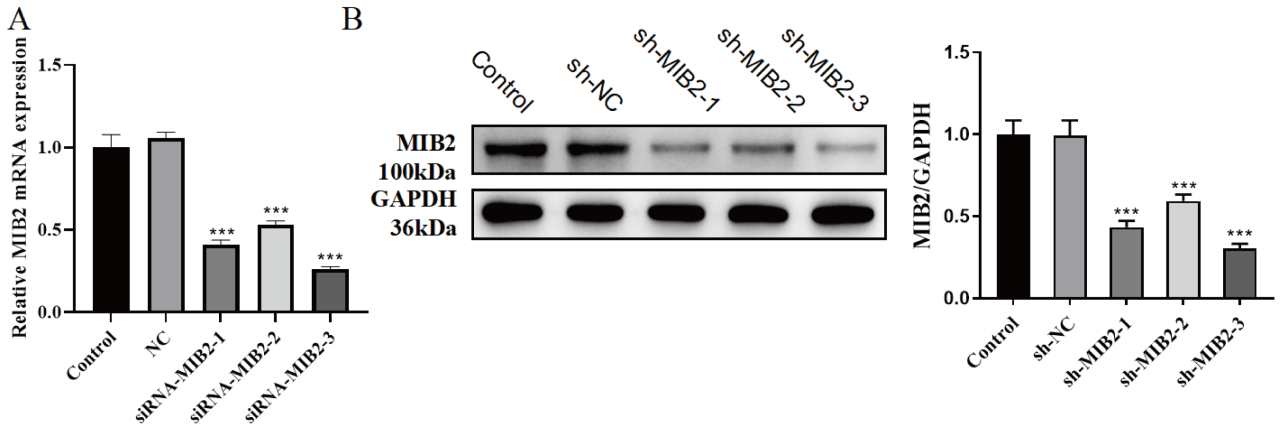

Fig. 3. Verification of the transfection efficiency of sh-MIB2 in HK-2 cells. (A) RT-qPCR was used to detect the mRNA knockdown efficiency of *MIB2* in HK-2 cells of each group. (B) Western blotting (WB) was utilized to assess the protein knockdown efficiency of MIB2 in HK-2 cells of each group. ***$p < 0.001$ vs sh-NC, $n = 3$.

0.001). This finding was confirmed by Western blot results (Fig. 3B) that MIB2 protein expression was markedly downregulated in the sh-MIB2 group relative to the sh-NC group ($p < 0.001$). Among the three sh-MIB2 sequences, sh-MIB2-3 resulted in the most significant reduction in mRNA (Fig. 3A) and protein levels of MIB2 (Fig. 3B) compared to sh-NC. Therefore, sh-MIB2-3 was selected for subsequent functional experiments. These results collectively indicate that sh-MIB2 effectively knocks down MIB2 expression in HK-2 cells.

Effect of MIB2 Knockdown on HK-2 Cell Proliferation Through GPX4 Regulation

RT-qPCR analysis (Fig. 4A) demonstrated that compared to the LPS+sh-NC group, the LPS+sh-MIB2 group exhibited significantly reduced *MIB2* mRNA levels and significantly elevated *GPX4* mRNA levels ($p < 0.001$); following co-treatment with RSL3 (a GPX4 inhibitor) in the LPS+sh-MIB2+RSL3 group, *GPX4* mRNA levels were markedly decreased relative to the LPS+sh-MIB2 group ($p < 0.001$). Western blot results (Fig. 4B) aligned with the mRNA trends, further confirming that MIB2 knockdown upregulated GPX4 protein expression—an effect reversed by RSL3. Phase-contrast microscopy combined with CCK-8 assay (Fig. 4C) revealed significantly enhanced cell viability in the LPS+sh-MIB2 group versus the LPS+sh-NC group ($p < 0.001$), whereas the LPS+sh-MIB2+RSL3 group showed significantly reduced viability compared to the LPS+sh-MIB2 group ($p < 0.001$).

Effect of MIB2 Knockdown on Ferroptosis of HK-2 Cells Through GPX4 Regulation

Detection of ROS using DCFH-DA fluorescent probe (Fig. 5A,B) revealed that intracellular ROS and oxidized lipids levels were significantly reduced in the LPS+sh-MIB2 group compared to the LPS+sh-NC group ($p < 0.001$), whereas the LPS+sh-MIB2+RSL3 group exhibited significantly elevated ROS levels relative to the LPS+sh-MIB2 group ($p < 0.01$). Iron assay (Fig. 5C) demonstrated that intracellular Fe^{2+} content was significantly decreased in the LPS+sh-MIB2 group versus the LPS+sh-NC group ($p < 0.001$)—an effect partially reversed by RSL3 co-treatment. ELISA analysis (Fig. 5D,E) showed significantly lower MDA and higher GSH content in the LPS+sh-MIB2 group than in the LPS+sh-NC group ($p < 0.001$), while the LPS+sh-MIB2+RSL3 group displayed significantly increased MDA and significantly decreased GSH content compared to the LPS+sh-MIB2 group ($p < 0.001$).

Effects of MIB2 Knockdown on Mitochondrial Function-Related Indexes in HK-2 Cells by Regulating GPX4

Transmission electron microscopy (TEM) observation (Fig. 6A) revealed improved mitochondrial morphology with more organized cristae structure in the LPS+sh-MIB2 group compared to the LPS+sh-NC group, whereas the LPS+sh-MIB2+RSL3 group exhibited renewed mitochondrial disorganization similar to the LPS+sh-NC group. Quantitative analysis (Fig. 6B,C) demonstrated that both the proportion of mitochondria with intact dense cristae and cristae length were significantly increased in the LPS+sh-MIB2 group versus the LPS+sh-NC group ($p < 0.001$), and RSL3 co-treatment significantly reversed this effect ($p < 0.01$). JC-1 staining (Fig. 6D) showed significantly elevated mitochondrial membrane potential in the LPS+sh-MIB2 group relative to the LPS+sh-NC group ($p < 0.001$), which was markedly reduced by RSL3 administration ($p < 0.001$). Chemiluminescence assay (Fig. 6E) indicated significantly increased intracellular ATP content in the LPS+sh-MIB2 group compared to the LPS+sh-NC group ($p < 0.001$), while RSL3 treatment substantially decreased ATP levels ($p < 0.001$).

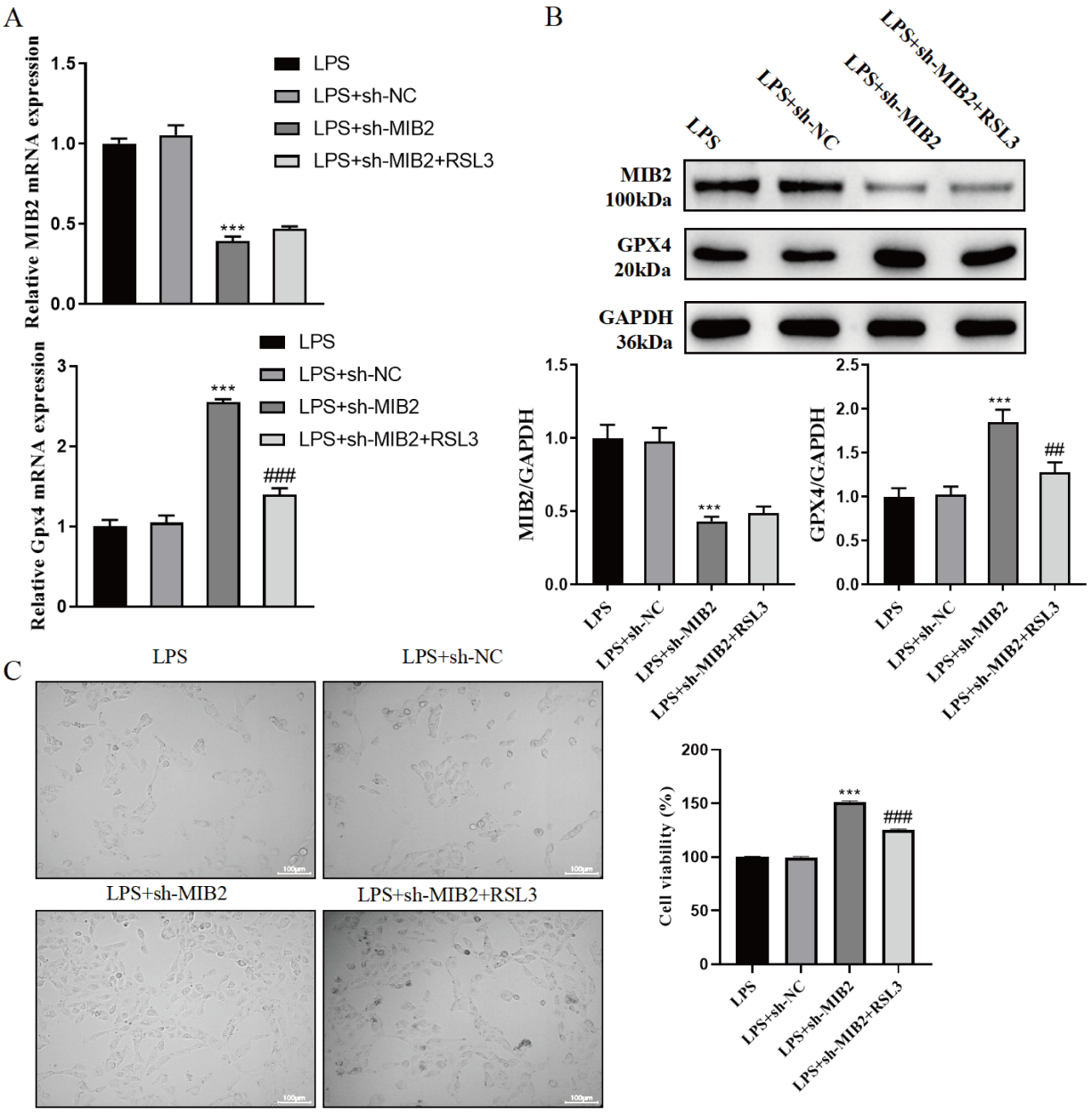

Fig. 4. MIB2 knockdown inhibits HK-2 cell proliferation via GPX4 regulation. (A) RT-qPCR was employed to detect the mRNA expression levels of *MIB2* and *GPX4*. (B) WB was used to detect the expression levels of MIB2 and GPX4 proteins. (C) Cell images of each group observed under an optical microscope and statistical analysis of cell survival rate measured using CCK-8. ***$p < 0.001$ vs LPS+sh-NC; $^{\#\#}p < 0.01$, $^{\#\#\#}p < 0.001$ vs LPS+sh-MIB2, $n = 3$.

Discussion

This study identifies a novel mechanism in SA-AKI whereby the E3 ubiquitin ligase MIB2 exacerbates renal tubular epithelial cell injury by promoting ferroptosis and mitochondrial dysfunction, via direct ubiquitination and degradation of GPX4. These findings expand our understanding of post-translational regulation of ferroptosis in SA-AKI, a critical clinical condition with incompletely defined pathophysiology [24,25].

Our results demonstrate that LPS treatment, a well-established approach to creating *in vitro* model of sepsis, significantly upregulates MIB2 expression while downregulating GPX4 in HK-2 cells. This inverse expression pattern, coupled with the direct interaction between MIB2 and GPX4 confirmed by Co-IP, strongly suggests that MIB2 may target GPX4 for degradation. Functional experiments further support this: knockdown of MIB2 reversed LPS-induced GPX4 downregulation, reduced ferroptosis markers (ROS, Fe^{2+}, MDA), improved mitochondrial morphol-

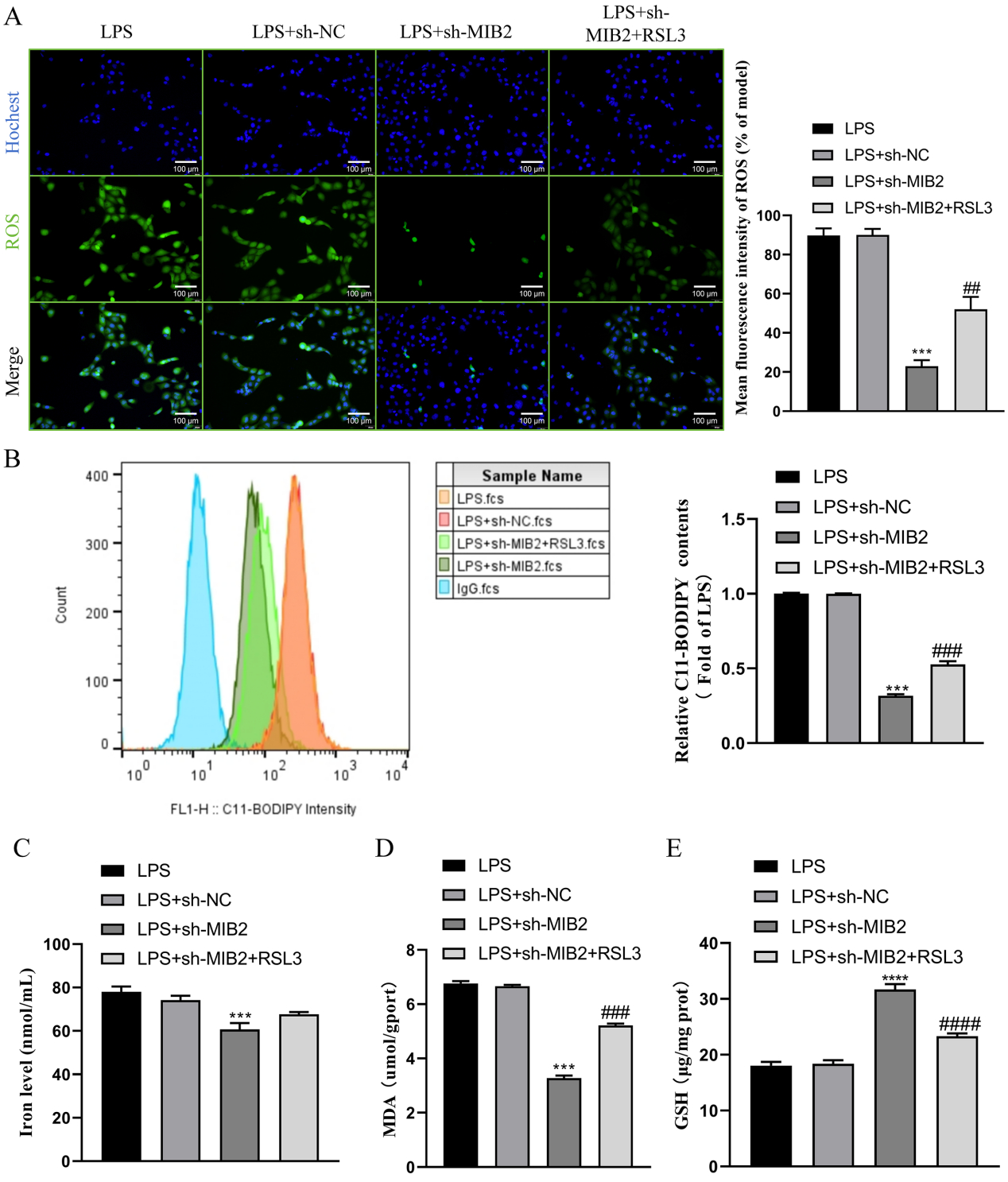

Fig. 5. MIB2 knockdown inhibits ferroptosis of HK-2 cells via GPX4 regulation. (A) Detect of intracellular ROS (green fluorescence) levels in HK-2 cells using DCFH-DA fluorescent probe, with the relative fluorescence intensity of ROS shown on the right. (B) Flow cytometry was used to detect oxidized lipids levels in HK-2 cells. (C) Iron ion detection kit was used to measure the intracellular iron content. (D,E) MDA and GSH assay kits were utilized to detect intracellular MDA and GSH contents. ***$p < 0.001$, ****$p < 0.0001$, vs LPS+sh-NC; $^{\#\#}p < 0.01$, $^{\#\#\#}p < 0.001$, $^{\#\#\#\#}p < 0.0001$ vs LPS+sh-MIB2, $n = 3$.

ogy and function, and enhanced cell viability. Importantly, these protective effects were abrogated by the GPX4 inhibitor RSL3, confirming that GPX4 is a critical downstream effector of MIB2 in SA-AKI. Notably, this regula-

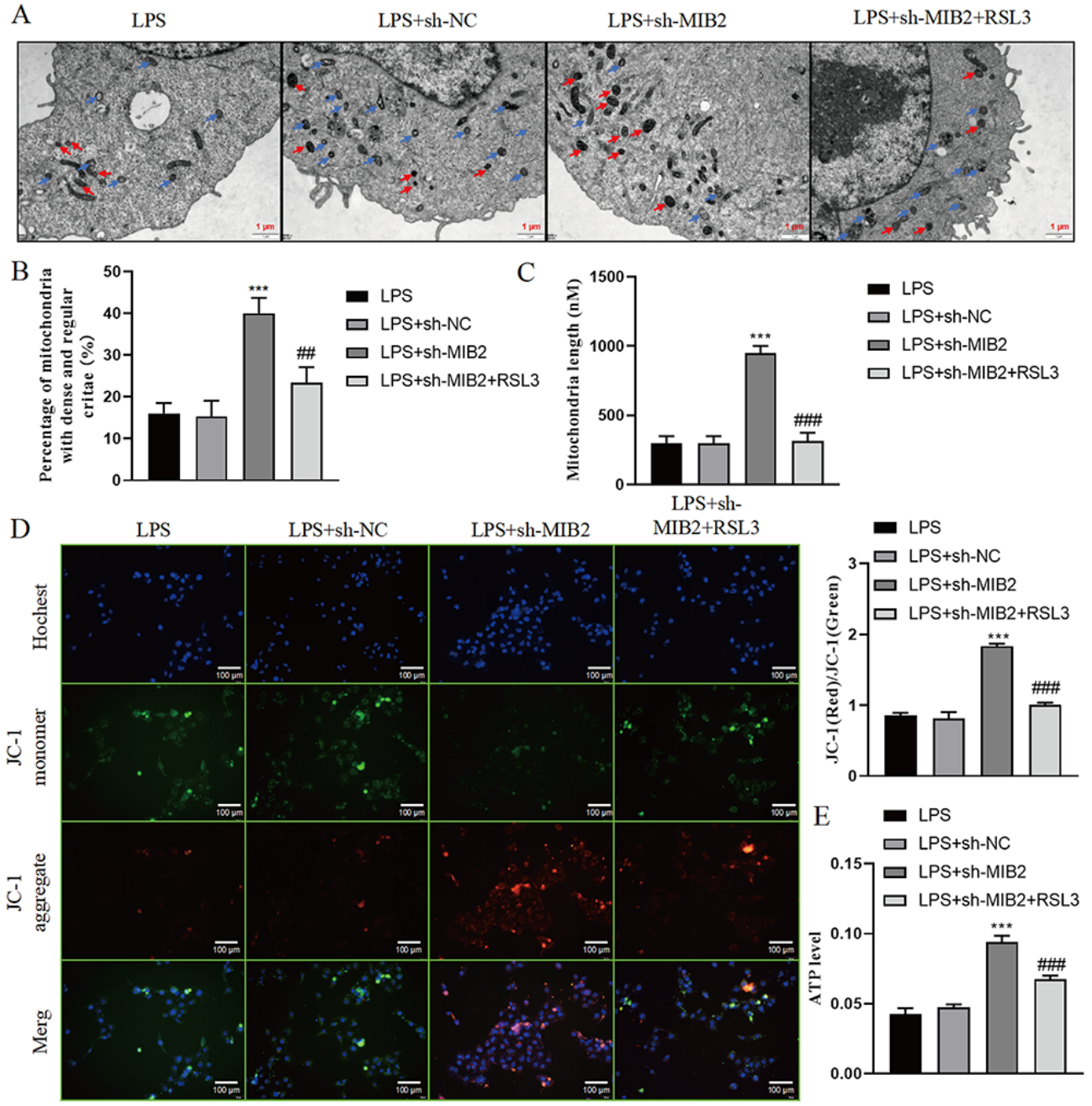

Fig. 6. MIB2 knockdown affects mitochondrial function-related indicators in HK-2 cells through GPX4 regulation. (A) TEM observation of mitochondrial morphology in HK-2 cells. Red arrow: intact mitochondrial cristae; Blue arrow: disrupted cristae and swollen mitochondria. (B,C) The proportion (B) and length of mitochondria (C) featuring fine and dense cristae. (D) JC-1 staining was used to detect mitochondrial membrane potential collapse. (E) Detection of intracellular ATP content using chemiluminescence method. ***$p < 0.001$ vs LPS+sh-NC; $^{\#\#}p < 0.01$, $^{\#\#\#}p < 0.001$ vs LPS+sh-MIB2, $n = 3$.

tory axis also involves transcriptional modulation, as observed in our analysis of *GPX4* mRNA levels.

Notably, MIB2 knockdown increased both protein and mRNA expression of GPX4 (Fig. 4), which we interpret as a dual regulatory mode: MIB2 directly promotes GPX4 ubiquitination/degradation (core mechanism), while indirectly modulating GPX4 transcription via regulation of septic-induced transcriptional repressors. This coordinated regulation explains the parallel elevation of GPX4 mRNA and protein, with MIB2-mediated ubiquitination remaining the primary effector.

Our findings have three key implications: (i) MIB2 is identified as a novel E3 ligase for GPX4, adding to the repertoire of post-translational regulators of ferroptosis in SA-AKI. (ii) There is a functional crosstalk between ferroptosis and mitochondrial dysfunction in SA-AKI, with GPX4 as a convergence point, and MIB2 as an upstream regulator of this crosstalk. (iii) MIB2 represents a potential therapeutic target, as its inhibition could stabilize GPX4, thereby mitigating ferroptosis and mitochondrial dysfunction, offering higher specificity than broad-spectrum ferroptosis inhibitors.

Our work aligns with and extends prior studies on GPX4 regulation and SA-AKI. For example, while TRIM21 [15] and HSP90 [26] regulate GPX4 stability via other pathways, our study uniquely identifies MIB2 as an E3 ligase that directly ubiquitinates GPX4 in SA-AKI, uncovering a new post-translational regulatory node specific to this condition. Notably, Zhou *et al.* [27] highlighted transcriptional regulation of GPX4 in SA-AKI, whereas our work reveals a complementary post-translational mechanism, demonstrating that GPX4 is regulated at both the transcriptional and post-translational levels in septic renal injury.

Notably, a recent study linked MIB2 to ferroptosis in sevoflurane-induced neuronal damage [28]; however, our work differs by focusing on SA-AKI and defining the molecular basis—GPX4 ubiquitination—thereby expanding MIB2's pathogenic role to renal injury. Collectively, these comparisons underscore the specificity of MIB2-GPX4 axis in SA-AKI and its potential as a unique therapeutic target.

However, several limitations exist. First, our experiments were conducted *in vitro* using HK-2 cells; *in vivo* validation using MIB2 knockout or conditional knockout mouse models of SA-AKI is necessary to confirm the physiological relevance. Second, the specific ubiquitination sites on GPX4 targeted by MIB2 and the type of ubiquitin chain (e.g., K48 vs. K63) remain undefined, requiring further biochemical analysis. Third, we did not explore whether MIB2 affects other ferroptosis-related proteins (e.g., SLC7A11) or mitochondrial regulators, which could expand our understanding of its role in SA-AKI. Fourth, we did not explore the upstream signaling pathways driving LPS-induced MIB2 upregulation. It is well established that LPS activates gene expression in kidney cells primarily through classical pathways such as TLR4, NF-κB, or MAPK. Future studies could employ specific inhibitors (e.g., TAK-242 to block TLR4, BAY 11-7082 to block NF-κB) in functional experiments to ascertain if these pathways are responsible for LPS-induced MIB2 upregulation.

Conclusions

In summary, our study demonstrates that MIB2 exacerbates SA-AKI by promoting GPX4 degradation, leading to ferroptosis and mitochondrial dysfunction in renal tubular epithelial cells. Targeting MIB2 may represent a novel strategy to preserve GPX4 activity and alleviate SA-AKI, but further preclinical investigations are warranted for validating our findings.

Abbreviations

DMEM, Dulbecco's Modified Eagle Medium; SA-AKI, sepsis-associated acute kidney injury; STR, short tandem repeat; sh-MIB2, shRNA targeting MIB2; SD, standard deviation; GPX4, glutathione peroxidase 4; GSH, glutathione; LPS, lipopolysaccharide; WB, Western blotting; Co-IP, co-immunoprecipitation; RT-qPCR, reverse-transcription polymerase chain reaction; ROS, reactive oxygen species; MDA, malondialdehyde; TEM, transmission electron microscopy; MIB2, mind bomb 2; FBS, fetal bovine serum; PS, penicillin-streptomycin.

Availability of Data and Materials

The datasets generated and analyzed during this study are available from the corresponding author upon reasonable request.

Author Contributions

The authors confirm contribution to the paper as follows: study conception and design: YJ; data collection: YW, LT, FZ; analysis and interpretation of results: YW, LT, FZ; draft manuscript: YW, LT, YJ. All authors contributed to critical revision of the manuscript for important intellectual content. All authors reviewed the results and approved the final version of the manuscript. All authors have participated sufficiently in the work and agreed to be accountable for all aspects of the work.

Ethics Approval and Consent to Participate

Not applicable.

Acknowledgment

Not applicable.

Funding

This work was supported by Natural Science Foundation of Liaoning, China (No. 2023-MS-259).

Conflict of Interest

The authors declare no conflict of interest.

References

[1] Li LF, Liu YY, Lin SW, Chang CH, Chen NH, Hung CY, *et al*. Low-Molecular-Weight Heparin Reduces Ventilation-Induced Lung Injury through Hypoxia Inducible Factor-1α in a Murine Endotoxemia Model. International Journal of Molecular Sciences. 2020; 21: 3097. https://doi.org/10.3390/ijms21093097.

[2] Poston JT, Koyner JL. Sepsis associated acute kidney injury. BMJ (Clinical Research Ed.). 2019; 364: k4891. https://doi.org/10.1136/bmj.k4891.

[3] Manrique-Caballero CL, Del Rio-Pertuz G, Gomez H. Sepsis-Associated Acute Kidney Injury. Critical Care Clinics. 2021; 37: 279–301. https://doi.org/10.1016/j.ccc.2020.11.010.

[4] Tong SYC, Venkatesh B, McCreary EK. Acute Kidney Injury With Empirical Antibiotics for Sepsis. JAMA. 2023; 330: 1531–1533. https://doi.org/10.1001/jama.2023.18591.

[5] Zarbock A, Nadim MK, Pickkers P, Gomez H, Bell S, Joannidis M, *et al*. Sepsis-associated acute kidney injury: consensus report of the 28th Acute Disease Quality Initiative workgroup. Nature Reviews. Nephrology. 2023; 19: 401–417. https://doi.org/10.1038/s41581-023-00683-3.

[6] Balakrishna A, Walco J, Billings FT, 4th, Lopez MG. Perioperative Acute Kidney Injury: Implications, Approach, Prevention. Advances in Anesthesia. 2023; 41: 205–224. https://doi.org/10.1016/j.aan.2023.06.005.

[7] Ostermann M, Lumlertgul N, Jeong R, See E, Joannidis M, James M. Acute kidney injury. Lancet (London, England). 2025; 405: 241–256. https://doi.org/10.1016/S0140-6736(24)02385-7.

[8] Peerapornratana S, Manrique-Caballero CL, Gómez H, Kellum JA. Acute kidney injury from sepsis: current concepts, epidemiology, pathophysiology, prevention and treatment. Kidney International. 2019; 96: 1083–1099. https://doi.org/10.1016/j.kint.2019.05.026.

[9] Cui J, Bai X, Chen X. Autophagy and Acute Kidney Injury. Advances in Experimental Medicine and Biology. 2020; 1207: 469–480. https://doi.org/10.1007/978-981-15-4272-5_34.

[10] Hu Y, Han J, Ding S, Liu S, Wang H. Identification of ferroptosis-associated biomarkers for the potential diagnosis and treatment of postmenopausal osteoporosis. Frontiers in Endocrinology. 2022; 13: 986384. https://doi.org/10.3389/fendo.2022.986384.

[11] Xie Y, Kang R, Klionsky DJ, Tang D. GPX4 in cell death, autophagy, and disease. Autophagy. 2023; 19: 2621–2638. https://doi.org/10.1080/15548627.2023.2218764.

[12] Zhang L, Chen F, Dong J, Wang R, Bi G, Xu D, *et al*. HDAC3 aberration-incurred GPX4 suppression drives renal ferroptosis and AKI-CKD progression. Redox Biology. 2023; 68: 102939. https://doi.org/10.1016/j.redox.2023.102939.

[13] Deng Z, Wang Y, Liu J, Zhang H, Zhou L, Zhao H, *et al*. WBP2 restrains the lysosomal degradation of GPX4 to inhibit ferroptosis in cisplatin-induced acute kidney injury. Redox Biology. 2023; 65: 102826. https://doi.org/10.1016/j.redox.2023.102826.

[14] Popovic D, Vucic D, Dikic I. Ubiquitination in disease pathogenesis and treatment. Nature Medicine. 2014; 20: 1242–1253. https://doi.org/10.1038/nm.3739.

[15] Sun X, Huang N, Li P, Dong X, Yang J, Zhang X, *et al*. TRIM21 ubiquitylates GPX4 and promotes ferroptosis to aggravate ischemia/reperfusion-induced acute kidney injury. Life Sciences. 2023; 321: 121608. https://doi.org/10.1016/j.lfs.2023.121608.

[16] Sun Y, Fan Y, Wang Z, Li M, Su D, Liu Y, *et al*. S100A16 promotes acute kidney injury by activating HRD1-induced ubiquitination and degradation of GSK3β and CK1α. Cellular and Molecular Life Sciences: CMLS. 2022; 79: 184. https://doi.org/10.1007/s00018-022-04213-5.

[17] Chen Q, Zheng W, Guan J, Liu H, Dan Y, Zhu L, *et al*. SOCS2-enhanced ubiquitination of SLC7A11 promotes ferroptosis and radiosensitization in hepatocellular carcinoma. Cell Death and Differentiation. 2023; 30: 137–151. https://doi.org/10.1038/s41418-022-01051-7.

[18] Ding Y, Chen X, Liu C, Ge W, Wang Q, Hao X, *et al*. Identification of a small molecule as inducer of ferroptosis and apoptosis through ubiquitination of GPX4 in triple negative breast cancer cells. Journal of Hematology & Oncology. 2021; 14: 19. https://doi.org/10.1186/s13045-020-01016-8.

[19] Wang Z, Shen N, Wang Z, Yu L, Yang S, Wang Y, *et al*. TRIM3 facilitates ferroptosis in non-small cell lung cancer through promoting SLC7A11/xCT K11-linked ubiquitination and degradation. Cell Death and Differentiation. 2024; 31: 53–64. https://doi.org/10.1038/s41418-023-01239-5.

[20] Yang X, Chen Y, Guo J, Li J, Zhang P, Yang H, *et al*. Polydopamine Nanoparticles Targeting Ferroptosis Mitigate Intervertebral Disc Degeneration Via Reactive Oxygen Species Depletion, Iron Ions Chelation, and GPX4 Ubiquitination Suppression. Advanced Science (Weinheim, Baden-Wurttemberg, Germany). 2023; 10: e2207216. https://doi.org/10.1002/advs.202207216.

[21] Guo Y, Chi X, Qu S, Sun Y, Liu J, Zhang L, *et al*. E3 ubiquitin-protein ligase 2 inhibits cell proliferation, migration, and invasion of non-small cell lung cancer through ubiquitination of Notch1. Acta Histochemica. 2022; 124: 151818. https://doi.org/10.1016/j.acthis.2021.151818.

[22] Huang F, Wang Y, Lv X, Huang C. WTAP-mediated N6-methyladenosine modification promotes the inflammation, mitochondrial damage and ferroptosis of kidney tubular epithelial cells in acute kidney injury by regulating LMNB1 expression and activating NF-κB and JAK2/STAT3 pathways. Journal of Bioenergetics and Biomembranes. 2024; 56: 285–296. https://doi.org/10.1007/s10863-024-10015-0.

[23] Zhang J, Zhang Y, Xiao F, Liu Y, Wang J, Gao H,*et al*. The peroxisome proliferator-activated receptor γ agonist pioglitazone prevents NF-κB activation in cisplatin nephrotoxicity through the reduction of p65 acetylation via the AMPK-SIRT1/p300 pathway. Biochemical Pharmacology. 2016; 101: 100–111. https://doi.org/10.1016/j.bcp.2015.11.027.

[24] Cecconi M, Evans L, Levy M, Rhodes A. Sepsis and septic shock. Lancet (London, England). 2018; 392: 75–87. https://doi.org/10.1016/S0140-6736(18)30696-2.

[25] Huang M, Cai S, Su J. The Pathogenesis of Sepsis and Potential Therapeutic Targets. International Journal of Molecular Sciences. 2019; 20: 5376. https://doi.org/10.3390/ijms20215376.

[26] Li Z, Wang X, Peng Y, Yin H, Yu S, Zhang W, *et al*. *Nlrp3* Deficiency Alleviates Lipopolysaccharide-Induced Acute Kidney Injury via Suppressing Renal Inflammation and Ferroptosis in Mice. Biology. 2023; 12: 1188. https://doi.org/10.3390/biology12091188.

[27] Zhou P, Zhao C, Chen Y, Liu X, Wu C, Hu Z. Klotho activation of Nrf2 inhibits the ferroptosis signaling pathway to ameliorate sepsis-associated acute kidney injury. Translational Andrology and Urology. 2023; 12: 1871–1884. https://doi.org/10.21037/tau-23-573.

[28] Zhao L, Gong H, Huang H, Tuerhong G, Xia H. Participation of Mind Bomb-2 in Sevoflurane Anesthesia Induces Cognitive Impairment in Aged Mice via Modulating Ferroptosis. ACS Chemical Neuroscience. 2021; 12: 2399–2408. https://doi.org/10.1021/acschemneuro.1c00131.